Modeling the interplay of thermal effects and transverse mode behavior in native-oxide-confined vertical-cavity surface-emitting lasers

T. Rössler, R. A. Indik, G. K. Harkness,* and J. V. Moloney
Department of Mathematics, University of Arizona, Tucson, Arizona 85721

C. Z. Ning
NASA Ames Research Center, T27A-1, Moffett Field, California 94035-1000

(Received 9 April 1998)

We present a microscopically based vertical-cavity surface-emitting laser (VCSEL) model that treats plasma and lattice heating self-consistently and includes gain dispersion in a fashion facilitating the incorporation of many-body effects. This model is used to investigate the interplay of thermal effects and transverse mode behavior observed in recent experiments with large-aperture selectively oxidized VCSELs. We confirm that the highly divergent single-mode emission seen experimentally at low ambient temperatures may be caused by a redshift of the cavity resonance frequency relative to the quantum-well gain peak. Moreover, due to the dependence of the gain spectrum on temperature our model qualitatively reproduces the measured *increase* of the dominant spatial scale of the low-temperature steady-state field patterns with pumping. Finally, we demonstrate that spatial hole burning plays a significant role at larger ambient temperatures and explains the *decrease* of the spatial wavelength with pumping, in agreement with the experiments.
[S1050-2947(98)02410-X]

PACS number(s): 42.55.Px, 42.55.Sa, 42.60.Jf

I. INTRODUCTION

Narrow circular beam divergence, single longitudinal mode operation, and dense two-dimensional packing capability are listed as the most advantageous characteristics of vertical-cavity surface-emitting lasers (VCSELs) in a 1988 review article [1] on the topic of surface-emitting semiconductor lasers. A very recent review [2] reiterates these points and highlights the advances in VCSEL design, fabrication, and performance achieved in the past decade. The fact that recently an entire conference [3] was dedicated to this particular optoelectronic device establishes most convincingly the technological importance VCSELs have gained. VCSELs are already being used commercially for high-speed medium-distance data links, and potential future applications encompass areas as diverse as optical storage, print heads, and bar-code scanners [4].

To a large extent, the use of selective oxidation of high aluminum content $Al_xGa_{1-x}As$ layers in the VCSEL structure [5,6] — to provide both current and optical mode confinement — is responsible for the great improvements in VCSEL performance in the last several years [6–11]. These so-called ''selectively oxidized'' or ''native-oxide confined'' VCSELs have thus attained a prominent status in the field, and a thorough understanding of their properties is desirable. Of particular interest for high-power applications is the potential for scaling to broad-area devices. In this context, the important role of thermal effects in the formation of transverse field patterns has been demonstrated by recent experiments [12] with large-aperture native-oxide confined VCSELs. Pumped just above threshold at an ambient temperature of 290 K, a 25 μm $\times$ 25 μm VCSEL exhibits highly divergent off-axis emission in a single mode, and the near field is characterized by parallel stripes corresponding to alternating regions of high and low intensity with a transverse spatial wavelength of ≈ 1 μm. With increasing pumping, this gives way to multimode behavior and more complex spatial field patterns with *longer* dominant wavelengths. In contrast, at larger ambient temperatures the measured near-threshold field exhibits multimode behavior and is dominated by large spatial scales that *decrease* with increasing pumping.

Clearly, a rigorous modeling of these phenomena poses a challenging task by requiring a simultaneous treatment of thermal effects and transverse mode behavior. Moreover, the high-order transverse modes seen in the experiments have to be included, and the femtosecond time scale of the polarization dynamics needs to be resolved in order to account for mode discrimination via gain dispersion. Several different types of models for VCSELs have already been discussed in the literature. Some of them [13–17] are predominantly concerned with the thermal aspects of VCSEL operation, while others [18–22] mostly concentrate on transverse mode behavior. Of the latter models, all employ a transverse modal decomposition of the electric field, including at most three modes. To our best knowledge, only the models presented in Refs. [23–26] seriously address both issues simultaneously. However, Refs. [23] and [26] lack concrete results for the full models, while the applicability of the otherwise excellent model of Ref. [24] is restricted to small-area VCSELs, since it relies on an expansion of the electric field in a small number (five) of transverse optical modes. Similarly, in Ref. [25] only two modes are taken into account. Moreover, the assumed linear carrier density dependence of the optical gain restricts the validity of the model to the vicinity of the

*Present address: Department of Physics and Applied Physics, University of Strathclyde, Glasgow G4 0NG, Scotland.

threshold and gain dispersion is not included.

We have previously established a VCSEL model [27] that employs a self-consistent approach to thermal effects. The temperatures of the plasma (T_p) and the lattice (T_l) are distinguished and treated as dynamical variables, coupled to the optical field, polarization, and carrier density. Pumping, stimulated emission, and relaxation towards T_l determine the evolution of T_p. In turn, the T_l dynamics are governed by coupling to T_p, ohmic heating, nonradiative recombination, and relaxation towards a fixed ambient temperature. Increasing T_l causes band-gap shrinkage, which directly affects the optical properties by redshifting the gain spectrum. This model exhibits the output power switchoff at stronger pumping typical in VCSELs [27], offers plasma heating as a microscopic justification of intensity-dependent gain in semiconductors [28], and predicts bistable operation of VCSELs at low ambient temperatures [29].

In order to model broad-area selectively oxidized VCSELs, three important extensions have been made: (i) We allow for an arbitrary two-dimensional transverse spatial dependence of the optical field in the active region—not relying on a modal expansion; (ii) we include a spatially varying transverse refractive index profile, motivated by the effective index model [24,30]; and (iii) we account for gain dispersion by treating the polarization dynamics within an effective Bloch equation approach [31]. Although we are restricting ourselves to the free-carrier model in this paper, we would like to note that the latter method greatly facilitates the incorporation of many-body effects. Applying this improved VCSEL model to the type of device studied in Ref. [12], we obtain qualitative agreement with the experiments in the following main points: (i) At a low ambient temperature and just above threshold the model exhibits highly divergent single-mode emission. As the pumping is increased, lasing occurs in several modes at *smaller* transverse wave vectors. (ii) In contrast, at a higher ambient temperature and just above threshold the steady-state field is dominated by small transverse wave vectors. With increasing pumping, *larger* transverse wave vectors appear, but the highly divergent off-axis emission seen at low temperatures is not observed.

Within our model, this behavior is readily explained: (i) Near threshold, the low ambient temperature regime is characterized by a pronounced redshift of the cavity resonance frequency relative to the gain peak frequency. We find that in such a case a laser with a sufficiently strong transverse index guide will select the standing wave lasing solution with finite transverse wave vector emitting at the gain peak frequency, in generalization of earlier results for traveling waves in unidirectional ring lasers [32]. Increased pumping raises the temperature of the gain medium, which results in a redshift of the gain spectrum and thus a reduced gain offset. Lasing still occurs preferentially at the gain peak frequency, hence stronger pumping leads to lasing at *smaller* transverse wave vectors. (ii) At larger ambient temperatures, the redshift just above threshold is reduced significantly or can even turn into a blueshift. In such a case, lasing occurs at near-zero wave vectors, again in accordance with the theory of Ref. [32]. Fields with such small wave vectors cause large-scale transverse modulations of the carrier density and the temperatures that can no longer be smoothed by diffusion. The resulting spatial hole burning leads to multimode emission at *larger* transverse wave vectors with increased pumping.

The general equations constituting our VCSEL model are introduced in the following section. Section III then specifies the geometry and the parameters for the particular model considered in this paper. Our results are presented in Sec. IV, discussed in Sec. V, and the paper is summarized in Sec. VI. Two appendices provide additional details about the derivation of our model equations and our choice of model geometry.

II. MODEL EQUATIONS

In this section, we present the basic equations of our VCSEL model. First, we formulate the dynamics of the scalar electric field within the slowly varying envelope approximation. The general treatment presented here includes externally imposed index guiding as well as thermally induced index changes. The dynamics of the total carrier density and total carrier kinetic energy density are derived from the semiconductor Bloch equations within the free-carrier model, following Ref. [27]. In contrast to this earlier treatment, however, the polarization is not adiabatically eliminated. Instead, we apply the effective Bloch equation approach detailed in Ref. [31]. This allows us to include the total polarization as a dynamical variable, thus accounting for gain dispersion. Since it merely requires a Lorentzian fit of a given measured or calculated susceptibility, the effective Bloch equation approach is well suited for the inclusion of many-body effects [31]. However, in this first version of our VCSEL model we are restricting ourselves to the free-carrier case, leaving the numerically expensive many-body susceptibility calculations at numerous densities and temperatures to a future improved model. Generalizing the treatment of the carrier kinetic energy dynamics from Ref. [27] and transforming to a temperature description, we arrive at a closed set of equations for the electric field, total polarization, total carrier density, and plasma temperature. Finally, this set is supplemented by a phenomenological equation for the lattice temperature.

A. Scalar field equation

A complete description of the electric field in a VCSEL would have to account for its vector nature. Although such a rigorous approach has recently been used to obtain the cold-cavity vectorial eigenmodes of an air-post VCSEL [33], it would be difficult to include such a treatment in a realistic dynamical VCSEL model (for additional comments, see Ref. [34]). In order to avoid these complications, and since the emphasis of this paper is not on polarization effects, we treat the electric field $\mathcal{E}$ as a scalar quantity. However, in the comparison between the results of our model and the experiments of Ref. [12], we will return to this point. We furthermore assume that the space and time dependence of the electric field is given by

$$\mathcal{E}(x,y,z;t)=\overline{E}(x,y,z;t)\exp(-i\omega_c t)+\text{c.c.}$$
$$\equiv E(x,y;t)\sin(k_c z)\exp(-i\omega_c t)+\text{c.c.} \quad (1)$$

The fast time dependence is governed by the cavity resonance frequency ω_c and $E(x,y;t)$ describes the complex field envelope, which varies slowly in time and in the trans-

verse spatial directions x and y. The assumption of a standing sinusoidal wave spatial dependence on the longitudinal direction z [27] is motivated by two well-known characteristics of VCSELs: (i) Their short cavity guarantees single longitudinal mode operation, and (ii) the use of distributed Bragg reflectors (DBRs) as mirrors results in a very high finesse cavity. This simplification is akin to the mean field limit ubiquitous in solid state and gas laser theory. In such lasers, the justification of that approach for Fabry-Pérot-type cavities is usually difficult due to longitudinal hole-burning effects, while it is straightforward in quantum well VCSELs, where the longitudinal extent of the active region is small compared to the longitudinal wavelength. The longitudinal wave vector is related to the cavity resonance frequency via

$$\omega_c = \frac{c}{n_{\mathrm{cav}}} k_c , \tag{2}$$

where c is the speed of light in vacuum and n_{cav} is the predominant refractive index in the cavity.

Within the slowly varying envelope approximation [27,31,38], the time dependence of the field envelope is governed by

$$\dot{E} = \frac{ic^2}{2\omega_c n_b n_g} \nabla_\perp^2 E - \kappa E + \frac{i\omega_c}{2\epsilon_0 n_b n_g} \beta \frac{L_m}{L} P + \frac{i\omega_c}{n_g} \left[\Delta n_b(x,y) + \frac{\partial n_b}{\partial T_l} (T_l - T_0) \right] E. \tag{3}$$

Here, n_b and n_g are the reference phase and group refractive indices of the active material in the quantum well. The first term on the right hand side represents transverse diffraction, where $\nabla_\perp^2$ is the transverse Laplacian. The term proportional to κ accounts for cavity losses, which are assumed to be due to the mirrors only. We define [27]

$$\kappa \equiv \frac{c}{2Ln_{\mathrm{cav}}} \ln\left(\frac{1}{r_m}\right), \tag{4}$$

where L is the length of the cavity and r_m is the amplitude reflection coefficient of the emitting end of the VCSEL, while the other end is assumed to be totally reflecting. $P(x,y;t)$ is the slowly varying complex envelope of the total polarization $\mathcal{P}(x,y,z;t)$ in the active material, i.e.,

$$\begin{aligned} \mathcal{P}(x,y,z;t) &= \overline{P}(x,y,z;t)\exp(-i\omega_c t) + \text{c.c.} \\ &\equiv P(x,y;t)\sin(k_c z)\Theta(0.5L_m - |z|) \\ &\quad \times \exp(-i\omega_c t) + \text{c.c.}, \end{aligned} \tag{5}$$

where $\Theta(x)$ is the Heaviside function ensuring that the polarization is nonzero only within the longitudinal extent L_m of the active medium. Note that L_m can encompass several quantum wells. The corresponding term in Eq. (3) represents the coupling between the field and the active medium, where ϵ_0 is the permittivity of vacuum, β is an effective coupling constant [27], and L_m/L is a geometric confinement factor. Index guiding is included via the second to last term on the right-hand side, where $\Delta n_b(x,y)$ is the spatial deviation of the refractive index from n_b. Finally, thermally induced index changes are described by the last term, where T_l is the lattice temperature and $\partial n_b/\partial T_l$ is the change of n_b with temperature measured at a reference temperature T_0.

B. Carrier dynamics

1. Semiconductor Bloch equations

The equations for the carrier-field interaction are derived from the semiconductor Bloch equations for the wave vector resolved envelope polarization variables $p_{\mathbf{k}}$ and carrier distributions $n_{\alpha,\mathbf{k}}$ [27,31,39,40]

$$\dot{p}_{\mathbf{k}} = -[\gamma_2 + i(\omega_{\mathbf{k}} - \omega_c)]p_{\mathbf{k}} - i\Omega_{\mathbf{k}}(n_{e,\mathbf{k}} + n_{h,\mathbf{k}} - 1), \tag{6}$$

$$\dot{n}_{\alpha,\mathbf{k}} = \Lambda_{\alpha,\mathbf{k}} - \gamma_n n_{\alpha,\mathbf{k}} - \gamma_1(n_{\alpha,\mathbf{k}} - f_{\alpha,\mathbf{k}}) + i(\Omega_{\mathbf{k}} p_{\mathbf{k}}^* - \text{c.c.}), \tag{7}$$

where $\alpha = e,h$ denotes electrons and holes, γ_2 is the polarization dephasing rate, and γ_n is the nonradiative carrier recombination rate. γ_1 is the carrier-carrier relaxation rate towards quasiequilibrium Fermi-Dirac distributions $f_{\alpha,\mathbf{k}}$, characterized by a total carrier density $N = (1/V)\Sigma_{\mathbf{k}} f_{e,\mathbf{k}} = (1/V)\Sigma_{\mathbf{k}} f_{h,\mathbf{k}}$ and a plasma temperature T_p. In the free-carrier model, the optical transition energy is given by

$$\begin{aligned} \hbar\omega_{\mathbf{k}} &\equiv \varepsilon_g(T_l) + \varepsilon_{e,\mathbf{k}} + \varepsilon_{h,\mathbf{k}} \equiv \varepsilon_g(T_l) + \frac{\hbar^2 k^2}{2m_e} + \frac{\hbar^2 k^2}{2m_h} \\ &\equiv \varepsilon_g(T_l) + \frac{\hbar^2 k^2}{2m_r}, \end{aligned} \tag{8}$$

where m_e, m_h, and m_r are the effective electron, hole, and reduced mass, respectively, while ε_g is the band gap, which depends on the lattice temperature T_l via [41]

$$\varepsilon_g(T_l) = \varepsilon_g(0) - \frac{v_1 T_l^2}{T_l + v_2}, \tag{9}$$

where $\varepsilon_g(0)$, v_1, and v_2 are material parameters. Within the free-carrier model, the Rabi frequency is given by

$$\Omega_{\mathbf{k}} = \frac{1}{\hbar} \mu_{\mathbf{k}} \overline{E}(t), \tag{10}$$

where $\mu_{\mathbf{k}}$ is the dipole matrix element, which can be written as [39,40]

$$\mu_{\mathbf{k}} = \mu_0 \frac{\varepsilon_g}{\hbar\omega_{\mathbf{k}}}, \tag{11}$$

with a material-dependent parameter μ_0. Finally,

$$\Lambda_{\alpha,\mathbf{k}} = \gamma_n \overline{f}_{\alpha,\mathbf{k}} (1 - n_{\alpha,\mathbf{k}}) \tag{12}$$

represents the pumping by carrier injection, where $\overline{f}_{\alpha,\mathbf{k}}$ are Fermi-Dirac distributions at the lattice temperature T_l, since the injected carriers can be assumed to be in equilibrium with the lattice, while the factor $(1 - n_{\alpha,\mathbf{k}})$ describes the Pauli blocking of the injected carriers [27,40].

2. Polarization dynamics

The polarization dynamics has a femtosecond time scale — much faster than the dynamics of the electric field and the carrier distributions — and can often be assumed to adjust instantaneously on the time scale of the latter processes. This adiabatic elimination of the polarization is realized by setting the time derivative of the microscopic polarizations in Eq. (6) to zero. Pursuing this approach, one eventually arrives at the model equations presented in Ref. [27]. However, by ignoring the time dependence of the polarization, one eliminates the frequency dependence of the gain — the gain dispersion — which provides an important means for mode selection, as will be shown below. Moreover, as discussed in Ref. [32], including transverse diffraction of the optical field while adiabatically eliminating the polarization can result in an ill-posed mathematical problem, as exhibited numerically by grid-scale instabilities.

For a more complete description, instead of adiabatically eliminating the polarization, one should take its dynamics into account. Since it is computationally very expensive to treat the wave vector resolved microscopic polarizations, alternatively an effective Bloch equation approach has been derived for semiconductor lasers [31]. The total polarization

$$\overline{P}=\frac{1}{V}\sum_{\mathbf{k}}\ \mu_{\mathbf{k}}^{*}p_{\mathbf{k}} \tag{13}$$

is related to the electric field in the frequency domain via

$$\tilde{P}(\omega)=\epsilon_0 n_b^2\chi(\omega)\tilde{E}(\omega), \tag{14}$$

where we have dropped the sinusoidal longitudinal dependence, since it is assumed to be the same for polarization and field. Here, $\tilde{F}(\omega)$ indicates the Fourier transform of a quantity $F(t)$. In the most basic version of the effective Bloch equation approach, the calculated or measured susceptibility is fitted by a frequency-independent ''background'' contribution and a single Lorentzian

$$\chi(\omega)=\chi_0(N,T_p,T_l)+\chi_1(N,T_p,T_l,\omega), \tag{15}$$

where

$$\chi_1(N,T_p,T_l,\omega)=\frac{A(N,T_p,T_l)}{i\Gamma(N,T_p,T_l)+[\omega_c+\omega-\varepsilon_g(T_l)/\hbar-\delta(N,T_p,T_l)]}. \tag{16}$$

For the reasons given in Appendix A, the fitting parameters χ_0, A, Γ, and δ in general depend on N, T_p, and T_l. Next, we also decompose the polarization P into a sum of terms, such that $\tilde{P}(\omega)=\tilde{P}_0(\omega)+\tilde{P}_1(\omega)$, where

$$\tilde{P}_0(\omega)=\epsilon_0 n_b^2\chi_0(N,T_p,T_l)\tilde{E}(\omega), \tag{17}$$

$$\tilde{P}_1(\omega)=\epsilon_0 n_b^2\chi_1(N,T_p,T_l,\omega)\tilde{E}(\omega). \tag{18}$$

Fourier transforming these equations into the time domain, we obtain

$$P_0(t)=\epsilon_0 n_b^2\chi_0(N,T_p,T_l)E(t), \tag{19}$$

$$\dot{P}_1(t)=\{-\Gamma(N,T_p,T_l)+i[\omega_c-\varepsilon_g(T_l)/\hbar-\delta(N,T_p,T_l)]\}P_1(t)-i\epsilon_0 n_b^2 A(N,T_p,T_l)E(t). \tag{20}$$

As discussed in Ref. [31], in performing the Fourier transformations, we have neglected the slow time evolution of the fitting parameters χ_0, A, Γ, and δ due to their dependence on N, T_p, and T_l. This is a good approximation as long as these quantities change slowly on the time scale of the inverse gain bandwidth, which is typically true in semiconductor lasers.

In the particular application of the effective Bloch equation approach presented here, we have evaluated the quantum well free-carrier model susceptibility Eq. (A2) using a two-dimensional density-of-states including spin degrees of freedom for the wave vector summation, as described in the Appendix of Ref. [27]. This susceptibility was then fitted for various total carrier densities N and plasma temperatures T_p at a fixed lattice temperature T_l. The only lattice temperature dependence we included was the thermal shift of the band gap. Since this is the main effect of T_l on the susceptibility, we found that this simplified fitting procedure gave satisfactory results at all relevant T_l. Finally, we note that compared to the situation discussed in Ref. [31], the fitting procedure in our case was complicated by the fact that the free-electron quantum well gain spectrum is much more asymmetric than its many-body counterpart. Since at the same time the application for VCSEL modeling requires fitting over a wide frequency range, our fits are not as tight as the ones shown in Ref. [31], but sufficient for the type of qualitative understanding aimed at in this article. An improvement of the quality of our fits can be expected when many-body effects are included.

3. Total carrier density

The dynamical equation for the total carrier density is obtained by summing Eq. (7) over all states and dividing by the total volume. Following Ref. [27], we define the total injected carrier density as $N_p\equiv(1/V)\Sigma_{\mathbf{k}}\overline{f}_{\alpha,\mathbf{k}}$. Due to Pauli blocking, only a fraction $N_0=\eta_N N_p$ of the injected carriers reaches the active region, where the density quantum efficiency is defined as

$$\eta_N\equiv\frac{1}{N_p V}\sum_{\mathbf{k}}\ \overline{f}_{\alpha,\mathbf{k}}(1-f_{\alpha,\mathbf{k}}). \tag{21}$$

Making use of Eq. (13) and the fact that carrier-carrier scattering processes do not change the total carrier density, we obtain

$$\dot{N} = -\gamma_n(N-N_0) + \frac{i}{\hbar}(\overline{P}^*\overline{E} - \text{c.c.}). \tag{22}$$

Averaging over the longitudinal direction and adding a diffusion term in order to account for the transverse spatial dependence we arrive at the final equation for the total carrier density

$$\dot{N} = D\nabla_\perp^2 N - \gamma_n[N - N_0\Xi_{\text{pump}}(x,y)] - \frac{\beta}{\hbar}\text{Im}(P^*E), \tag{23}$$

where D is the ambipolar carrier diffusion constant and $\Xi_{\text{pump}}(x,y)$ is the externally imposed spatial pumping profile, for instance, due to current confinement.

4. Plasma temperature

In order to obtain a dynamical equation for the plasma temperature, we first determine an equation for the total electron kinetic energy density $W \equiv (1/V)\Sigma_{\mathbf{k}}\varepsilon_{e,\mathbf{k}}n_{e,\mathbf{k}}$. As detailed in Ref. [27], this is achieved by multiplying Eq. (7) by $\varepsilon_{e,\mathbf{k}}$, summing over all states, and dividing by the total volume. In analogy to the treatment in Sec. II B 3, we define the total injected electron energy density as $W_p \equiv (1/V)\Sigma_{\mathbf{k}}\varepsilon_{e,\mathbf{k}}\overline{f}_{e,\mathbf{k}}$. Again, due to Pauli blocking only the fraction $W_0 = \eta_W W_p$ of the injected electron kinetic energy density reaches the active region, where the kinetic energy density quantum efficiency is defined as

$$\eta_W \equiv \frac{1}{W_p V}\sum_{\mathbf{k}} \varepsilon_{e,\mathbf{k}}\overline{f}_{e,\mathbf{k}}(1-f_{e,\mathbf{k}}). \tag{24}$$

Since carrier-carrier scattering processes also do not change the total carrier kinetic energy density, which is related to the total electron kinetic energy density simply by a constant factor in our model, we obtain

$$\dot{W} = -\gamma_n(W-W_0) + \frac{i}{\hbar}\left(\frac{1}{V}\sum_{\mathbf{k}} \mu_{\mathbf{k}}\varepsilon_{e,\mathbf{k}}p_{\mathbf{k}}^*\overline{E} - \text{c.c.}\right). \tag{25}$$

As shown in Appendix A, we can generalize the approach of Ref. [27] and rewrite the term in the last bracket in order to obtain a closed set of equations. This leads to

$$\dot{W} = -\gamma_n(W-W_0) - \frac{2}{\hbar}\frac{m_r}{m_e}\text{Im}\{[\hbar(\omega_c - i\gamma_2) - \varepsilon_g]\overline{P}^*(t)\overline{E}(t) - i\hbar\dot{\overline{P}}^*(t)\overline{E}(t)\}. \tag{26}$$

We now make a variable transformation to obtain an equation for the plasma temperature T_p [27]. Combining Eqs. (22) and (26) yields

$$\dot{T}_p = -\gamma_n[J_W(W-W_0) - J_N(N-N_0)] - J_W\frac{2}{\hbar}\frac{m_r}{m_e}\text{Im}\{[\hbar(\omega_c - i\gamma_2) - \varepsilon_g]\overline{P}^*(t)\overline{E}(t) - i\hbar\dot{\overline{P}}^*(t)\overline{E}(t)\} + J_N\frac{2}{\hbar}\text{Im}(\overline{P}^*\overline{E}), \tag{27}$$

where [27]

$$J_W \equiv \frac{\partial N}{\partial \mu_e}\left(\frac{\partial W}{\partial T_p}\frac{\partial N}{\partial \mu_e} - \frac{\partial W}{\partial \mu_e}\frac{\partial N}{\partial T_p}\right)^{-1}, \tag{28}$$

$$J_N \equiv \frac{\partial W}{\partial \mu_e}\left(\frac{\partial W}{\partial T_p}\frac{\partial N}{\partial \mu_e} - \frac{\partial W}{\partial \mu_e}\frac{\partial N}{\partial T_p}\right)^{-1}, \tag{29}$$

and μ_e is the electronic chemical potential. As in Sec. II B 3, we average over the longitudinal direction, add a diffusion term, and take the pumping profile into account. Furthermore, we include a phenomenological coupling term between plasma and lattice temperature due to carrier-phonon scattering [27] to arrive at the final equation for the plasma temperature

$$\dot{T}_p = D\nabla_\perp^2 T_p - \gamma_n\{J_W[W - W_0\Xi_{\text{pump}}(x,y)] - J_N[N - N_0\Xi_{\text{pump}}(x,y)]\} - J_W\frac{\beta}{\hbar}\frac{m_r}{m_e}\text{Im}\{[\hbar(\omega_c - i\gamma_2) - \varepsilon_g]P^*E - i\hbar\dot{P}^*E\} + J_N\frac{\beta}{\hbar}\text{Im}(P^*E) - \gamma_T(T_p - T_l), \tag{30}$$

where the plasma temperature diffusion is assumed to be governed by the same diffusion constant D as the carrier density diffusion, and γ_T is the rate of plasma cooling. In our simulations we find that the dominant contribution to the plasma heating is due to kinetic energy pumping with Pauli blocking. However, far above threshold stimulated emission can be of equal importance. This is in agreement with previous studies of carrier heating in microcavity lasers [42].

C. Lattice temperature

To complete our model, we supplement the above set of equations by an entirely phenomenological dynamical equation for the lattice temperature, namely [27],

$$\dot{T}_l = D_T\nabla_\perp^2 T_l + \gamma_T\frac{C_p}{C_l}(T_p - T_l) - \gamma_a(T_l - T_a) + \gamma_n\frac{\hbar\omega_c N}{C_l} + \frac{SRj^2}{C_l L}. \tag{31}$$

Here, D_T is the thermal diffusivity, $C_p = \partial W/\partial T_p$ and C_l are the plasma and lattice specific heat capacities, respectively, γ_a is the cooling rate towards a fixed ambient temperature T_a, S is the device area, R is the total device resistance, and $j = eL_m\gamma_n N_p$ is the current density. The second to last and last terms represent nonradiative recombination and Joule heating, respectively.

TABLE I. Parameters used in the VCSEL simulations.

Parameter	Symbol	Value
Cavity resonance wavelength in vacuum	λ_0	870.0 nm
Refractive indices: GaAs (phase), GaAs (group), $Al_{0.2}Ga_{0.8}As$	n_b, n_g, n_{cav}	3.65, 4.30, 3.50
Index step	Δn_b	-0.05
Cavity length, quantum well width	L, L_{well}	248.6 nm, 10 nm
Longitudinal extent of active region	$L_m = 3L_{\mathrm{well}}$	30 nm
Amplitude reflection coefficient	r_m	0.9998
Effective coupling constant	β	0.09312
Linear thermal index change (GaAs at $T_0 = 300$ K)	$\frac{\partial n_b}{\partial T_l}$	4.0×10^{-4} K^{-1}
Polarization dephasing rate	γ_2	1.0×10^{13} s^{-1}
Nonradiative carrier recombination rate	γ_n	1.0×10^{9} s^{-1}
Effective masses (GaAs): electron, hole	m_e, m_k	$0.0665m_0$, $0.4500m_0$
Zero temperature bandgap (bulk GaAs)	$\varepsilon_g(0)$	1.519 eV
Thermal bandgap shift parameters (GaAs)	v_1, v_2	5.405×10^{-4} eV/K, 204 K
Dipole matrix element parameter	μ_0	$5e$ Å
Carrier diffusion constant (GaAs)	D	1.0×10^{-3} $\mathrm{m^2\,s^{-1}}$
Rate of plasma cooling	γ_T	$1.0\times10^{12}\,\mathrm{s^{-1}}$
Thermal diffusivity (GaAs)	D_T	$1.3055\times10^{-4}\,\mathrm{m^2\,s^{-1}}$
Lattice specific heat capacity	C_l	1.7388 $\mathrm{J\,K^{-1}\,m^{-3}}$
Rate of lattice cooling	γ_a	$1.0\times10^{8}\,\mathrm{s^{-1}}$
Device area	S	625 $\mu\mathrm{m}^2$
Total device resistance	R	1000 Ω

III. MODEL SPECIFICATIONS AND NUMERICAL METHODS

In the choice of our model geometry and the model parameters we have tried to remain as true as possible to the actual device used in the experiments of Ref. [12]. However, since certain device specifications were not available, we were occasionally forced to resort to generic values. The specific set of parameters chosen for the numerical implementation of the equations of Sec. II is summarized in Table I. Note that although the devices were measured to emit around 850 nm [12], we have fixed the cavity resonance at 870 nm. This discrepancy is necessitated by the fact that we are using the bulk band gap in our optical model, whereas the active region consists in fact of quantum wells. The energy shift of the lowest-order confined states in a 10-nm GaAs quantum well increases the band gap by several tens of meV. In order to compensate for the different band gap, we intentionally reduced the cavity resonance frequency.

The model geometry is indicated in Fig. 1, which depicts a cross section in the x-z plane at the center of the device with respect to y. The y-z cross section at the center with respect to x is identical, with one exception: The lateral extent of the active region and the cladding in the y direction is taken to be 25 μm, instead of the 27 μm used for the x direction. Viewed from above, this corresponds to a slightly rectangular active region. The reasons for introducing this asymmetry are detailed in Appendix B. In the longitudinal direction, the active medium encompasses three 100-Å GaAs quantum wells, placed in the center of the λ cavity assumed to consist of $Al_{0.2}Ga_{0.8}As$. In Fig. 1, the top and bottom DBRs are depicted as black horizontal bars. Within the effective index model [24,30], the oxidized high Al content layers in the DBR structure result in an effective index step. This transverse index step is taken to be $\Delta n = -0.05$, in accordance with the value given in Ref. [12], and the location of the index step coincides with the transverse border of the active region. The oxide aperture also provides current confinement and is believed to lead to highly uniform current injection. We therefore assume carrier pumping with a constant pumping carrier density N_p within the transverse extent of the active region and zero outside. Our computational domain encompasses 50 $\mu\mathrm{m} \times 50$ μm with a spatial grid of 128×128 points. We are using a spectral method to evaluate the transverse spatial derivatives, hence periodic boundary conditions are applied implicitly. However, this is irrelevant since our computational domain is large enough such that near its boundary all variables attain spatially constant values.

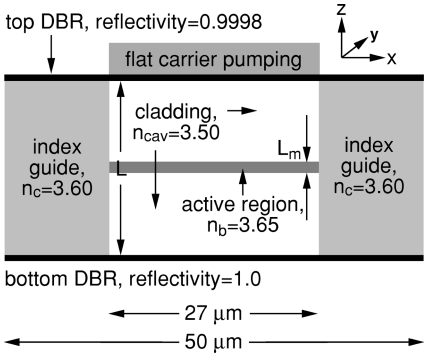

FIG. 1. Schematic of the device geometry used in our study. Shown is an x-z cross section at $y = 0$. The various symbols are explained in the text and additional parameter values are provided in Table I.

The time evolution of the quantities E, P, N, T_p, and T_l according to the model equations given in Sec. II is computed with a split-step operator method. First, the part of the time evolution mediated by the transverse derivatives in our model equations is evaluated spectrally, using fast Fourier transforms. The second operator comprises the remainder of the model equations. Note that the equations for E and P — when considered independent from the remaining equations — are linear with slowly varying coefficients depending on the slowly changing variables N, T_p, and T_l. Therefore, we use the following scheme for the second operator: Keeping N, T_p, and T_l constant at their previous values during one time step, we can solve exactly for the next values of E and P by propagating the coupled equations via multiplication with an exponential of a complex matrix. Since we are using very small time steps (to resolve the P dynamics we need $\Delta t \approx 0.5/\Gamma_1 \approx 15$ fs), we are making only a small mistake by holding N, T_p, and T_l constant during the propagation of E and P (see Ref. [43] for more details). Simultaneously, we propagate N, T_p, and T_l to their next values using a first order explicit Euler method, with E and P fixed at their previous values. For a given set of input parameters, and starting from some initial conditions, the simulation is performed until the spatial averages of N, T_p, and T_l have converged to a near constant value. The length of the simulations is hence determined by the longest time constant in our model, namely, the inverse of the relaxation rate γ_a of the lattice temperature to the ambient temperature. Since $1/\gamma_a = 10$ ns, our simulations usually extended over several tens of nanoseconds.

IV. RESULTS

In this section, we present the results of our model calculations for two different ambient temperatures T_a and discuss the dependence on the pumping carrier density N_p. Comparing our simulations with the experiments of Ref. [12], we find qualitative agreement in the near-field behavior just above threshold and the dependence of the dominant length scales on pumping.

A. Low ambient temperature: 290 K

The most striking experimental observation of Ref. [12] is the appearance of a deeply modulated ''roll-like'' near-field intensity pattern just above threshold for low heat ' sink temperatures. In order to investigate this regime, we chose an ambient temperature $T_a = 290$ K and varied the pumping density to find the threshold value. At $N_p = 3.65 \times 10^{24}$ m^{-3} no steady lasing was observed, but at $N_p = 3.67 \times 10^{24}$ m^{-3} we find a steady-state lasing solution. Figures 2(a) and 2(b) show a 30-ps time average of the corresponding near- and far-field intensities, respectively. Note that the length of intervals for time averages in this paper was chosen such that they encompass several periods of the slowest field oscillations. As in the experiment, the time-averaged near field consists of rolls and has a transverse spatial wavelength of about 0.9 μm. The time-averaged far field given in Fig. 2(b) exhibits a double spot at $(k_x, k_y) = (\pm k_{\max}, 0)$ indicating that on average the field is a standing wave in x with negligible spatial structure in y. Furthermore,

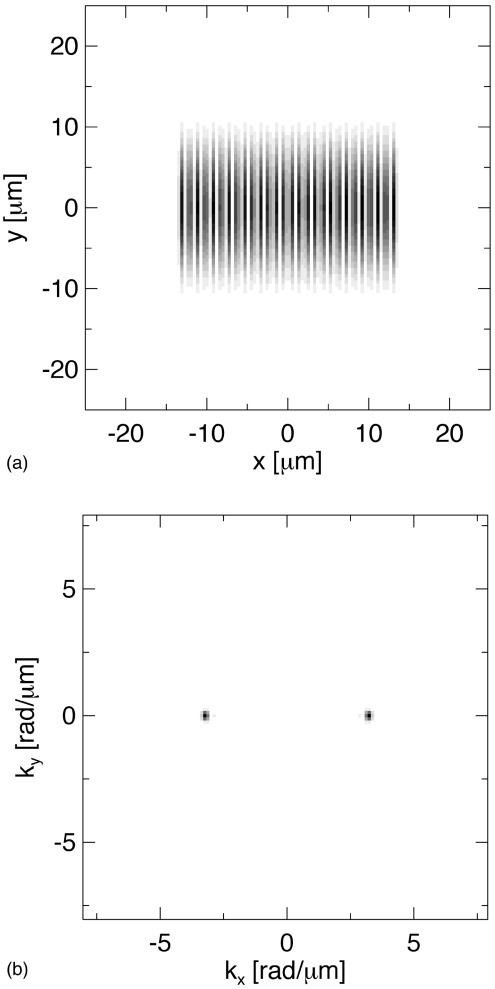

FIG. 2. Time-averaged near-field (a) and far-field (b) intensities at low ambient temperature $T_a = 290$ K and pumped just above threshold ($N_p = 3.67 \times 10^{24}$ m^{-3}). The near-field intensity (a) exhibits a roll pattern with a spatial wavelength of approximately 0.9 μm. The corresponding time-averaged far field (b) consists of a symmetric double spot characteristic for a standing wave with a single wave vector. In both figures, higher intensity values are shown as darker regions.

a spectral analysis of the time dependence of the spatially averaged near field yields a power spectrum with a narrow single peak. Thus, at threshold our model reproduces very well the single-mode highly divergent emission seen in the experiments.

As the pumping carrier density is increased from threshold in our model, the above simple single-mode lasing state gives way to multimode behavior and more complex spatial field patterns with larger dominant spatial scales. The latter is demonstrated in Fig. 3, where we display the dependence of the magnitude $k_{\max}$ of the dominant wave vector in the far field as a function of N_p. This increase of the dominant spatial wavelength of the near-field pattern and the presence of multiple frequencies is also in qualitative agreement with the experiments of Ref. [12].

The more detailed output field characteristics observed in our model and in the experiments start to deviate further above threshold. The experiments yield single-mode output at 1.05 times the threshold value and the fields predomi-

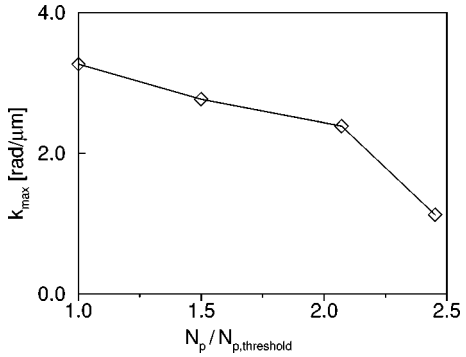

FIG. 3. As the pumping density N_p is increased from threshold for $T_a=290$ K, the magnitude of the dominant transverse wave vector $k_{\max}$ in the far field decreases.

nantly show structure in a single spatial direction for pumping as high as 1.3 times the threshold value. In contrast, the emission obtained from our model already has considerable contributions from several modes and shows structure in both spatial directions at 1.01 times the threshold. Possible reasons for this difference between experiment and simulations are discussed in Sec. V C below.

B. High ambient temperature: 330 K

Since the experiments revealed a very different behavior of the VCSELs at high ambient temperatures, we repeated our investigations at $T_a=330$ K. Figure 4 displays the steady-state lasing characteristics near threshold. Here, panels (a) and (b) show 150-ps time averages of the near-field intensity at threshold ($N_p=3.95\times10^{24}$ m^{-3}) and slightly above threshold ($N_p=4.00\times10^{24}$ m^{-3}), respectively. In comparison to the results at low ambient temperature, shown in Fig. 2(a), it is very apparent that the dominant spatial scale of the near fields in Fig. 4 is much larger. Correspondingly, the far field is peaked around zero wave vector. At threshold, the output field is completely dominated by the fundamental mode [Fig. 4(a)], but slightly above threshold several transverse modes are present [Fig. 4(b)]. This agrees with the observation in Ref. [12] that near threshold at higher heat sink temperatures the VCSEL favors emission at small divergence angles and exhibits multiple frequency components.

We also considered the effects of increased pumping at the higher ambient temperatures. The results we obtained for $N_p=9.00\times10^{24}$ m^{-3} are shown in Fig. 5. In contrast to the case of lower T_a, where the dominant spatial scale *increased* with N_p (see Fig. 3), we find that at higher ambient temperatures stronger pumping leads to *decreased* spatial wavelengths. However, the highly divergent emission seen at low T_a is not observed. Again, very similar behavior is reported in Ref. [12].

V. DISCUSSION

In the previous section, we have demonstrated that our model exhibits the same qualitative behavior as the experiments in several important aspects. We now proceed to analyze these results in terms of the features of our model, thus providing a theoretical interpretation of the experimentally observed behavior. Furthermore, we discuss deviations between the experiment and our simulations, and we indicate

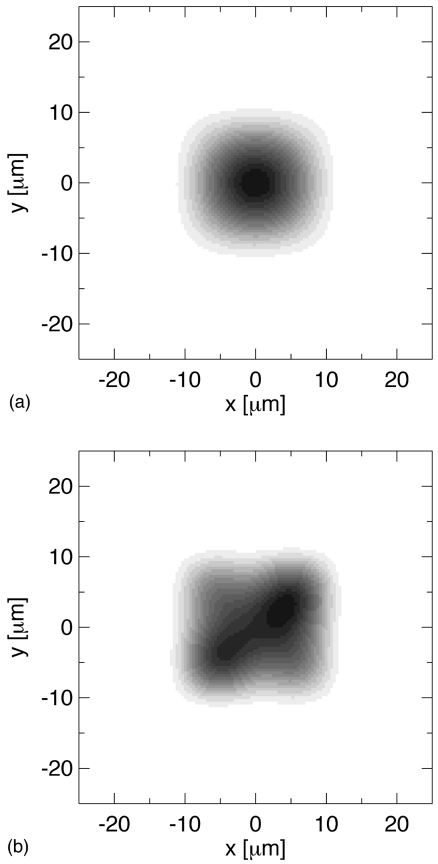

FIG. 4. Same as Fig. 2(a), but at a high ambient temperature $T_a=330$ K and for (a) pumping at threshold ($N_p=3.95\times10^{24}$ m^{-3}) and (b) slightly above threshold ($N_p=4.00\times10^{24}$ m^{-3}). At both pumping values the time-averaged near field intensity exhibits large spatial wavelengths of approximately 10 μm. The corresponding time-averaged far fields are peaked around zero wave vector.

the model improvements necessary in order to ameliorate the differences.

For a preliminary explanation of their experiments, the authors of Ref. [12] invoked a previous theoretical investigation [32] of the space-time dynamics of a homogeneously broadened, single-longitudinal-mode, unidirectional ring laser described by two-level Maxwell-Bloch equations. As shown in Ref. [32], near the lasing threshold the detuning between the cavity resonance frequency and the peak gain frequency determines the characteristics of the output field. A redshift of the cavity resonance frequency relative to the peak gain frequency results in a stable traveling wave lasing solution exhibiting a finite transverse wave vector such that its frequency *matches the peak gain frequency*. As the size of the redshift is reduced, the value of the transverse wave vector decreases in order to maintain the alignment of lasing frequency and gain peak. On the other hand, in the case of a blueshift lasing *occurs at the cavity resonance frequency*, with zero transverse wave vector. Note that for any size of the blueshift this constitutes the mode with the lowest possible frequency and therefore the maximum gain. To summarize, according to Ref. [32], the stable lasing solution corresponds to the transverse mode whose frequency maximizes the gain for a given detuning.

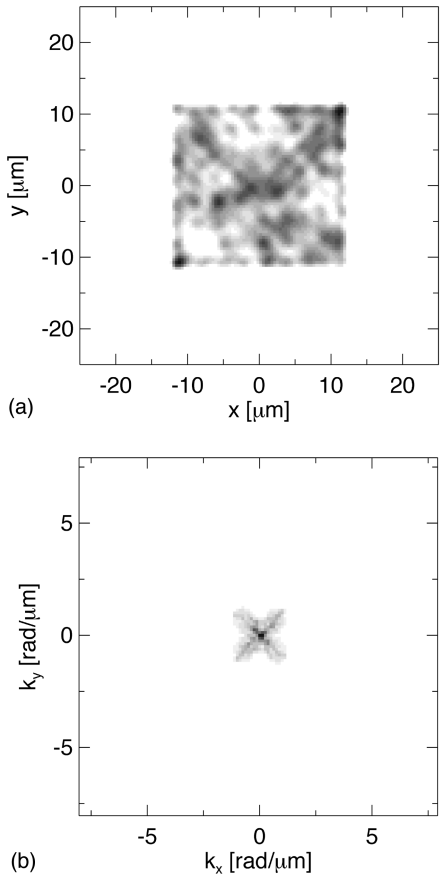

FIG. 5. Same as Fig. 2, but at a high ambient temperature $T_a = 330$ K and for pumping far above threshold ($N_p = 9.00 \times 10^{24}$ m^{-3}). The time-averaged near field intensity (a) exhibits smaller spatial wavelengths than near threshold (see Fig. 4). The corresponding time-averaged far field (b) shows large divergence angles, but not nearly as large as for low T_a [see Fig. 2(b)].

An influence of the sign of the gain offset on transverse mode behavior has indeed already been observed in VCSEL experiments [44,45]. In conjunction with the VCSELs well-known redshift of the gain peak with temperature [46], the increase of the dominant spatial scale of the near-threshold steady-state field pattern with heat sink temperature seen in the experiments of Ref. [12] may be expected based on the theory of Ref. [32]. However, a more complete description including the effects of index-guiding, the coupling of plasma and lattice temperatures, and spatial hole burning — such as provided by our VCSEL model — is necessary to reproduce the experimentally observed dependence on pumping.

A. Low ambient temperature: 290 K

The behavior at threshold for low ambient temperatures comes closest to being fully captured by the theory of Ref. [32]. Here, lasing occurs in a single mode with well-defined wave vector and frequency. In Fig. 6 we show the gain spectrum for $T_a = 290$ K and $N_p = 3.67 \times 10^{24}$ m^{-3}, evaluated from our Lorentzian fit for $\chi(\omega, N, T_p, T_l)$ using the temporal and spatial average values of N, T_p, and T_l within the active region. This procedure is well justified, since N, T_p, and T_l are nearly constant throughout the active region and

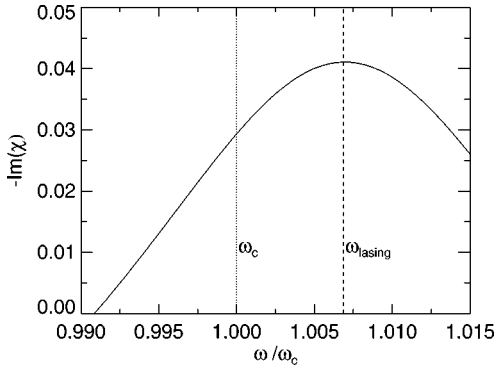

FIG. 6. Gain spectrum ($\propto -\mathrm{Im}\chi$) at low ambient temperature $T_a = 290$ K and pumped just above threshold ($N_p = 3.67 \times 10^{24}$ m^{-3}), computed from the Lorentzian fit and using the temporal and spatial averages of N, T_p, and T_l within the active region in order to evaluate the parameters χ_0, A, Γ, ε_g, and δ. The cavity resonance frequency ω_c is redshifted with respect to the gain peak frequency, but lasing occurs at the frequency ω_{lasing}, which lines up exactly with the gain peak.

hence the gain for a given transverse mode depends only very weakly on its spatial structure. As seen in Fig. 6, at this ambient temperature the cavity resonance frequency ω_c is redshifted with respect to the gain peak frequency, while the lasing frequency ω_{lasing} — computed from the power spectrum of the spatially averaged field — lines up with the gain peak. Hence, transverse mode selection is entirely due to the frequency criterion established in Ref. [32].

We note that due to index guiding in the native-oxide confined VCSELs, the steady-state field is a standing-wave mode [47] instead of one of the traveling-wave lasing solutions treated in Ref. [32]. The corresponding spatial dependence of the field intensity — which is absent for traveling waves — causes a transverse modulation of the carrier density. However, since the carrier diffusion length (1.0 μm) is comparable to the spatial wavelength of the field pattern ($\approx$0.9 μm) diffusion almost completely restores the spatial homogeneity of the carrier density. Furthermore, the transverse index guide supports only a finite number of bound modes, depending on the size of the index step. This results in an upper limit on the available mode frequencies. To confirm this effect, we performed studies with one transverse dimension. We found that for a given redshift the frequency selection criterion of Ref. [32] cannot be satisfied when the magnitude of the index step is reduced below a critical value.

While the theory of Ref. [32] applies strictly only for single-mode behavior near threshold, our model calculations reveal that at low ambient temperatures its predictions remain qualitatively valid even under multiple-mode operation above threshold: With increasing pumping the dominant lasing frequency remains near the gain peak, as exemplified by Fig. 7. Within our model, stronger pumping causes a rise of the lattice temperature and results in a redshift of the gain peak. Hence, for lasing to occur at the gain peak frequency, smaller transverse wave vectors are required. This explains the increase of the dominant spatial wavelength with pumping demonstrated in Fig. 3 and observed in the experiments.

B. High ambient temperature: 330 K

At higher ambient temperatures, we encounter a different situation. The small wave vector standing waves present near

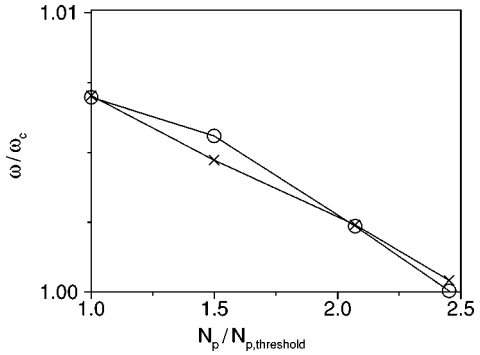

FIG. 7. As the pumping density N_p is increased from threshold for $T_a=290$ K, the dominant frequency in the steady state field (crosses) remains close to the gain peak frequency (circles).

threshold result in transverse modulations of the carrier density on very large spatial scales (≈ 10 μm), such that diffusion can no longer restore the spatial homogeneity. These spatial inhomogeneities in the carrier density (and the temperatures) translate into a spatial dependence of the susceptibility. Hence, the effective gain for a given transverse mode depends not only on the mode frequency, but also on the overlap of the mode pattern and the spatial gain profile.

A preliminary understanding of the transverse mode behavior can still be gained from considering the gain spectrum evaluated at the active-region averages of N, T_p, and T_l. Accordingly, Fig. 8 shows $-\mathrm{Im}(\chi)$ for $T_a=330$ K at threshold ($N_p=3.95\times10^{24}$ m^{-3}). In contrast to the low-temperature case depicted in Fig. 6, the cavity resonance frequency is blueshifted from the gain peak frequency. Under these circumstances, the theory of Ref. [32] predicts the mode with the lowest frequency as stable lasing solution. For periodic boundary conditions, this corresponds to the zero wave vector mode, whose frequency matches the cavity resonance [32]. Due to the finite extent of the index guide, in our model a homogeneous zero wave vector solution is not possible. Instead, the fundamental mode — corresponding to the index-guided mode with the smallest wave vector and therefore the smallest frequency— dominates the field pattern at threshold, as can be clearly seen from Fig. 4(a). We note that although it is still blueshifted from the gain peak, the dominant lasing frequency is red-shifted considerably from the cavity resonance. This is simply a consequence of thermally induced index changes included here, but not considered in Ref. [32]: The higher lattice temperature within the active region enhances the index guide, which results in a redshift of all transverse mode frequencies. Even with this redshift included, the frequency of the fundamental mode maximizes the active-region averaged gain. Hence, again the transverse mode selection at threshold is in accordance with the frequency criterion of Ref. [32].

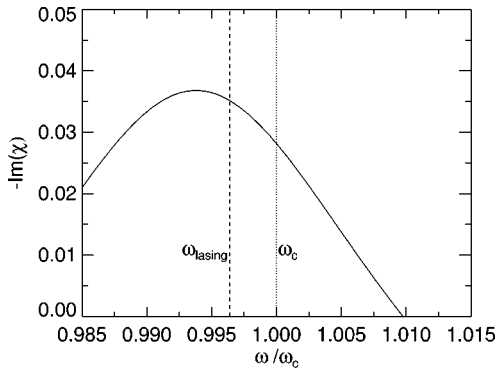

FIG. 8. Same as Fig. 6, but for $T_a=330$ K and $N_p=3.95\times10^{24}$ m^{-3}. The cavity resonance frequency ω_c is blueshifted with respect to the gain peak frequency, while the lasing frequency ω_{lasing} lies between the gain peak and the cavity resonance.

Slightly above threshold, multimode emission is observed, both in our simulations [see Fig. 4(b)] and in the experiments. Since the frequency spacing between adjacent transverse modes is small at near-zero wave vectors, so are the differences in gain. It is therefore not surprising that several transverse modes are simultaneously above threshold. In order to understand the observed outcome of the competition between these modes for the available gain, we have examined a strongly simplified version of our model. Assuming that only the fundamental and first excited transverse mode are above threshold, we write the total field as a linear superposition $E(x,y;t)=c_1(t)E_1(x,y)\exp(-i\omega_1 t)+c_2(t)E_2(x,y)\exp(-i\omega_2 t)$, where the complex coefficients c_i are slowly varying and $E_i(x,y)$ denotes the normalized mode patterns. Neglecting the slow time dependence of c_i and N in performing Fourier transformations, we arrive at the corresponding polarization

$$P(x,y;t)=\epsilon_0 n_b^2[\chi(\omega_1,N)c_1(t)E_1(x,y)\exp(-i\omega_1 t)+\chi(\omega_2,N)c_2(t)E_2(x,y)\exp(-i\omega_2 t)].$$

In the absence of carrier diffusion and for constant and homogeneous temperatures, the susceptibility depends on space only through the mode intensities: $\chi(\omega;x,y)=\chi(\omega;|c_1E_1(x,y)|^2,|c_2E_2(x,y)|^2)$. Here, we have omitted terms containing the beat frequency between the modes, which average to zero over the carrier relaxation time scale. For small intensities, we can approximate

$$\chi(\omega_i;x,y)\approx\chi^{(1)}(\omega_i)+\chi^{(3)}(\omega_i)[\chi^{(1)}(\omega_1)|c_1E_1(x,y)|^2+\chi^{(1)}(\omega_2)|c_2E_2(x,y)|^2].$$

We furthermore assume that the susceptibility is purely imaginary, i.e., we neglect carrier-induced refractive index changes. Considering the projection of the dynamical equation for the total field onto the two modes, we obtain coupled ordinary differential equations for the mode amplitudes, namely,

$$\dot{c}_1=\alpha_1 c_1-(\beta_{11}|c_1|^2+\beta_{12}|c_2|^2)c_1, \tag{32}$$

$$\dot{c}_2=\alpha_2 c_2-(\beta_{21}|c_1|^2+\beta_{22}|c_2|^2)c_2. \tag{33}$$

In these equations, $\alpha_i>0$ is the difference between linear gain and loss for mode i ($i=1,2$), $\beta_{ii}>0$ is the self-saturation coefficient, and $\beta_{ij}>0$ ($i\neq j$) is the cross-saturation coefficient. The exact same pair of equations has been discussed in the context of homogeneously broadened two-level atomic lasers [48]. The single-mode and two-mode steady-state solutions of these equations are readily obtained.

As shown in Ref. [48], their linear stability is governed by the relative size of the self- and cross-saturation coefficients. In our case, these coefficients depend on overlap integrals of the squares of the mode patterns. Using the Cauchy-Schwartz inequality, it is straightforward to show that $\beta_{12}\beta_{21} \leqslant \beta_{11}\beta_{22}$ is always satisfied. As a consequence, the only stable solution is characterized by the presence of both modes [48]. Based on the analysis of this simplified situation we conclude that the carrier-density mediated dependence of the gain on the field intensity — in other words, spatial hole burning — is responsible for the observed multimode behavior in our full model near threshold.

Finally, we discuss the dependence of the steady-state field patterns on pumping at high ambient temperatures. As the pumping is increased, the coupling between plasma and lattice temperatures leads to an even larger redshift of the gain peak relative to the cavity resonance frequency. According to the theory of Ref. [32], we would therefore expect lasing to continue to occur preferentially in the fundamental mode. This is indeed the case, but several larger wave-vector modes also appear in the output field, as shown in Fig. 5. At these higher pumping values many transverse modes are above threshold. Hence, an analysis similar to that presented in the previous paragraph, complicated by the presence of multiple, nondegenerate modes, would be necessary to understand the mode competition behavior. Such an analysis is beyond the scope of this paper. Nevertheless, we evaluated the overlap integrals of the squares of two arbitrary infinite index step waveguide mode patterns and found that the integrals appearing in the cross-saturation terms are always smaller than the corresponding integrals in the self-saturation terms. This leads us to believe that again spatial hole burning is the governing mechanism for the observed multimode behavior at increased pumping.

C. Discrepancies and possible model improvements

The most significant discrepancy between the experimental results and our simulations occurs at low ambient temperatures. As discussed in Sec. IV A, at pumping as low as 1.01 times the threshold value our model yields multimode steady-state fields having comparable large wave vectors in both transverse directions, while the experiments show single-mode lasing with large wave vectors in only one transverse direction for pumping up to 1.05 times the threshold value. Since the experiments also show that the linear polarization is aligned with the persisting ''rolls,'' we feel that this discrepancy can only be resolved by incorporating the vectorial nature of the field. Efforts in this direction are already under way. Moreover, once one accepts the fact that the modes with large wave vectors in only one transverse direction are favored, it is easier to understand why the low ambient temperature experiments yield single-mode lasing up to larger pumping values: The frequency spacing between these modes is significant, hence the mode discrimination according to frequency is very strong. This is in stark contrast to the high ambient temperature situation discussed in Sec. V B.

While our model qualitatively captures the main trends seen in the experiments, obviously a more quantitative analysis would require a description of the optical properties that goes beyond the free-carrier model used here. As emphasized earlier, the inclusion of many-body effects is in principle very straightforward within the effective Bloch equation approach. However, in order to obtain the Lorentzian fitting parameters over a wide range of carrier densities, plasma and lattice temperatures, a large number of numerically intensive many-body gain calculations are necessary before the simulations can be performed. This aspect of improving our model is also in progress.

Finally, the relaxation of the lattice temperature towards the ambient temperature is assumed to be described by Newton's law of cooling [see Eq. (31)]. It is not clear that such a simplified approach is indeed valid. Moreover, the corresponding temperature relaxation rate will strongly depend on the specific device geometry and can only be estimated. In the future, we intend to instead incorporate a more realistic description of the longitudinal lattice temperature transport.

VI. SUMMARY

We have introduced a dynamical VCSEL model that accounts for the intricate coupling between thermal effects and optical properties and includes the important transverse mode selection mechanism due to gain dispersion. For different ambient temperatures, this model qualitatively reproduces the near-field behavior just above threshold as well as the dependence of the dominant length scales on pumping seen in recent experiments with large-aperture native-oxide confined VCSELs [12]. An analysis of the results of our simulations in terms of the features of our model provides a theoretical interpretation of the experimental behavior.

More specifically, at *low* ambient temperatures and near threshold, highly divergent single-mode emission is observed both in the experiments and in our simulations. Within our model, this regime is characterized by a considerable redshift of the cavity resonance frequency relative to the peak frequency of the gain, where the latter is evaluated at the temporal and spatial averages of carrier density, plasma, and lattice temperatures. As predicted by a theory for homogeneously broadened, single-longitudinal-mode, unidirectional ring lasers [32], under such circumstances stable single-mode emission at large transverse wave vectors occurs and the lasing frequency lines up with the gain peak. The applicability of this theory to index-guided VCSELs is in this case justified by the fact that diffusion compensates the short wavelength modulation of the carrier density and plasma temperature caused by the spatial variation of the standing wave field intensity, thus restoring the spatial homogeneity of the system. As the pumping is increased at these low ambient temperatures, the dominant spatial wavelength of the steady-state field pattern becomes larger. Our model demonstrates that this behavior is caused by the coupling between thermal effects and optical properties: Stronger pumping increases the lattice temperature and therefore results in a redshift of the gain spectrum. Hence, for lasing to continue to occur at the gain peak frequency, increasingly smaller transverse wave vectors are required.

Near threshold, the measured steady-state field patterns at *high* ambient temperatures exhibit multimode behavior and are dominated by near-zero wave vectors. Again, our model reproduces these results. In this regime, the field-induced modulation of the carrier density and the plasma temperature

are on a large spatial scale, such that diffusion can no longer restore the spatial homogeneity. Nevertheless, using the gain spectrum evaluated at the temporally and spatially averaged carrier density and temperatures provides fundamental insight: Here, the cavity resonance is strongly blueshifted relative to the gain peak and according to the theory of Ref. [32] lasing in the lowest frequency mode is expected. With the observed domination of the fundamental mode, this prediction is substantiated. However, due to the spatial inhomogeneity of the system transverse modes are discriminated not only according to their frequency, but also according to their spatial mode patterns. Within a simplified model we show that the interplay of self- and cross-saturation of modes caused by spatial hole burning is responsible for the multimode emission seen near threshold. The same mechanism is argued to be at work at higher pumping levels, encouraging the appearance of higher-order modes. This explains the decrease of the dominant spatial wavelengths with increased pumping, which are obtained in the experiments and in our simulations.

Our studies have provided an understanding of the physical origin of the highly divergent emission seen in broad-area selectively oxidized VCSELs at low ambient temperatures. At the same time, they also indicate a possible approach for the suppression of these high-order transverse modes for high-power applications that require a narrow beam. As mentioned in Sec. V A, the size of the index step imposes an upper limit on the transverse wave vectors supported by the index guide. Since the effective index step is determined by the thickness and the placement of the oxide layer in the VCSEL structure [10], this effect could be utilized to control the maximal divergence angle.

ACKNOWLEDGMENTS

We thank the authors of Ref. [12] for providing their results prior to publication. T.R. acknowledges helpful discussions with Stephan Koch, Rolf Binder, Dariusz Burak, Michal Mlejnek, J. Kenton White, and Paul Pax. This work is supported by the U.S. Air Force Office of Scientific Research, Air Force Materiel Command, USAF, under Grant No. F49620-97-1-0002 and by NATO Collaborative Research Grant No. CRG 971186.

APPENDIX A: DERIVATION OF THE PLASMA TEMPERATURE EQUATION

This appendix provides more details of the derivation of the plasma temperature equation implemented in this paper. First, we invoke the quasiequilibrium approximation in Eq. (6), replacing the carrier distributions $n_{\alpha,\mathbf{k}}$ by quasiequilibrium Fermi-Dirac distributions $f_{\alpha,\mathbf{k}}$. Ignoring the slow time dependence of the $f_{\alpha,\mathbf{k}}$, we Fourier transform into the frequency domain and solve for the envelope polarizations. This yields

$$\tilde{p}_{\mathbf{k}}(\omega)=\frac{\mu_{\mathbf{k}}(1-f_{e,\mathbf{k}}-f_{h,\mathbf{k}})}{\hbar[(\omega_{\mathbf{k}}-\omega_c-\omega)-i\gamma_2]}\tilde{E}(\omega). \tag{A1}$$

Note that using the definition of the total polarization Eq. (13) we immediately obtain the susceptibility within the free-carrier model as

$$\chi(\omega)=\frac{1}{V\epsilon_0 n_b^2}\sum_{\mathbf{k}}\frac{|\mu_{\mathbf{k}}|^2(1-f_{e,\mathbf{k}}-f_{h,\mathbf{k}})}{\hbar[(\omega_{\mathbf{k}}-\omega_c-\omega)-i\gamma_2]}. \tag{A2}$$

The Fermi-Dirac distributions $f_{\alpha,\mathbf{k}}$ depend on the total carrier density N and the plasma temperature T_p, while the optical transition frequency $\omega_{\mathbf{k}}$ depends on the lattice temperature T_l. Therefore, the susceptibility is in general a function of all these quantities and the fitting parameters used within the effective Bloch equation approach of Sec. II B 2 have to reflect this dependence.

We can now use the expression for the microscopic polarization Eq. (A1) in Eq. (25). For this purpose, we Fourier transform the latter equation into frequency space and consider only the terms in the last bracket. The product of the time-dependent quantities $p_{\mathbf{k}}^*$ and $\bar{E}$ under Fourier transformation becomes a convolution, namely,

$$\int_{-\infty}^{+\infty}d\omega'\frac{1}{V}\sum_{\mathbf{k}}\mu_{\mathbf{k}}\varepsilon_{e,\mathbf{k}}\tilde{p}_{\mathbf{k}}^*(\omega)\tilde{\bar{E}}(\omega-\omega'), \tag{A3}$$

where we are focusing on the first term in the bracket only, since the second term is just the complex conjugate. Using the definition of the optical transition energy Eq. (8) and the quasiequilibrium result for the microscopic polarization Eq. (A1), we rewrite

$$\int_{-\infty}^{+\infty}d\omega'\frac{m_r}{m_e}\frac{1}{V}\sum_{\mathbf{k}}\frac{|\mu_{\mathbf{k}}|^2(\hbar\omega_{\mathbf{k}}-\varepsilon_g)(1-f_{e,\mathbf{k}}-f_{h,\mathbf{k}})}{\hbar[(\omega_{\mathbf{k}}-\omega_c-\omega)+i\gamma_2]}\tilde{\bar{E}}^*(\omega)\tilde{\bar{E}}(\omega-\omega'). \tag{A4}$$

Subtracting and adding $\hbar(\omega_c+\omega-i\gamma_2)$ in the numerator under the sum, this simplifies to

$$\int_{-\infty}^{+\infty}d\omega'\frac{m_r}{m_e}\left\{\frac{1}{V}\sum_{\mathbf{k}}|\mu_{\mathbf{k}}|^2(1-f_{e,\mathbf{k}}-f_{h,\mathbf{k}})\tilde{\bar{E}}^*(\omega)\tilde{\bar{E}}(\omega-\omega')\right.$$
$$\left.+[\hbar(\omega_c+\omega-i\gamma_2)-\varepsilon_g]\frac{1}{V}\sum_{\mathbf{k}}\frac{|\mu_{\mathbf{k}}|^2(1-f_{e,\mathbf{k}}-f_{h,\mathbf{k}})}{\hbar[(\omega_{\mathbf{k}}-\omega_c-\omega)+i\gamma_2]}\tilde{\bar{E}}^*(\omega)\tilde{\bar{E}}(\omega-\omega')\right\}. \tag{A5}$$

Using Eqs. (A1) and (13), we obtain

$$\int_{-\infty}^{+\infty}d\omega'\frac{m_r}{m_e}\left\{\frac{1}{V}\sum_{\mathbf{k}}|\mu_{\mathbf{k}}|^2(1-f_{e,\mathbf{k}}-f_{h,\mathbf{k}})\tilde{\bar{E}}^*(\omega)\tilde{\bar{E}}(\omega-\omega')+[\hbar(\omega_c+\omega-i\gamma_2)-\varepsilon_g]\tilde{\bar{P}}^*(\omega)\tilde{\bar{E}}(\omega-\omega')\right\}. \tag{A6}$$

and transforming back into the time domain yields

$$\frac{m_r}{m_e}\left\{\frac{1}{V}\sum_{\mathbf{k}}|\mu_{\mathbf{k}}|^2(1-f_{e,\mathbf{k}}-f_{h,\mathbf{k}})|\bar{E}(t)|^2+[\hbar(\omega_c-i\gamma_2)-\varepsilon_g]\bar{P}^*(t)\bar{E}(t)-i\hbar\dot{\bar{P}}^*(t)\bar{E}(t)\right\}. \tag{A7}$$

Inserting this back into Eq. (25), we note that the first term is real and therefore vanishes under subtraction of the complex conjugate. This leads to Eq. (26).

APPENDIX B: RECTANGULAR VERSUS SQUARE MODEL GEOMETRY

Nominally, the VCSELs used in the experiments of Ref. [12] have a square geometry. However, there are at least two physical mechanisms that can destroy an intended square spatial symmetry: (i) The fabrication of an index guide via selective oxidation may introduce a geometrical asymmetry. This was demonstrated impressively in Ref. [49] where the authors deduced the transverse dimensions of a supposedly square VCSEL from the measured subthreshold emission spectrum and found a 20% mismatch between the x and y extents. This type of cavity asymmetry would favor a particular linear polarization for a large range of pumping values [50], which is indeed the case for the experiments of Ref. [12]. (ii) The favoring of a particular linear polarization seen in the experiments can also be caused by crystal strains introduced during growth and processing [51]. For instance, in Ref. [50] it was reported that all the circular VCSELs from a given wafer were lasing in the same dominant polarization state. Therefore, crystal strains are a source of spatial asymmetry as well.

Considering the above points, we argue that it is in fact very likely that the actual device symmetry deviated from a perfect square. The most straightforward way to include this spatial asymmetry in our model was the use of a slightly rectangular active region, as detailed in Sec. III. As for the size of the x-y mismatch, we chose a value that is of the same order as that mentioned under (i). However, we note that both of the above symmetry-breaking mechanisms exhibit themselves through the selection of a preferred linear polarization. Therefore, a fully satisfactory treatment of the asymmetry would require a vectorial approach to the field.

[1] K. Iga, F. Koyama, and S. Kinoshita, IEEE J. Quantum Electron. **24**, 1845 (1988).

[2] W. W. Chow *et al.*, IEEE J. Quantum Electron. **33**, 1810 (1997).

[3] *Vertical-Cavity Surface-Emitting Lasers*, edited by K. D. Choquette, and D. G. Deppe, SPIE Proc. No. 3003 (SPIE, Bellingham, 1997).

[4] R. A. Morgan, see *Vertical-Cavity Surface-Emitting Lasers* (Ref. [3]), p. 14, and references therein.

[5] D. L. Huffaker, D. G. Deppe, K. Kumar, and T. J. Rogers, Appl. Phys. Lett. **65**, 97 (1994).

[6] K. D. Choquette, R. P. Schneider, Jr., K. L. Lear, and K. M. Geib, Electron. Lett. **30**, 2043 (1994).

[7] K. L. Lear *et al.*, Electron. Lett. **31**, 208 (1995).

[8] K. D. Choquette *et al.*, IEEE Photonics Technol. Lett. **7**, 1237 (1995).

[9] D. L. Huffaker, H. Deng, Q. Deng, and D. G. Deppe, Appl. Phys. Lett. **69**, 3477 (1996).

[10] K. D. Choquette *et al.*, Appl. Phys. Lett. **70**, 823 (1997).

[11] B. Weigl *et al.*, IEEE J. Sel. Top. Quantum Electron. **3**, 409 (1997).

[12] S. P. Hegarty *et al.*, in *Vertical-Cavity Surface-Emitting Lasers II*, edited by K. D. Choquette and R. A. Morgan, SPIE Proc. No. 3286 (SPIE, Bellingham, 1998), p. 198.

[13] W. Nakwaski and M. Osinski, IEEE J. Quantum Electron. **27**, 1391 (1991).

[14] J. W. Scott, S. W. Corzine, R. S. Geels, and L. A. Coldren, Appl. Phys. Lett. **62**, 1050 (1993); J. W. Scott, R. S. Geels, S. W. Corzine, and L. A. Coldren, IEEE J. Quantum Electron. **27**, 1391 (1993).

[15] R. Michalzik and K. J. Ebeling, IEEE J. Quantum Electron. **29**, 1963 (1993).

[16] J. Piprek, H. Wenzel, and G. Szefka, IEEE Photonics Technol. Lett. **6**, 139 (1994).

[17] Y.-G. Zhao and J. G. McInerney, IEEE J. Quantum Electron. **31**, 1668 (1995).

[18] M. Shimizu, F. Koyama, and K. Iga, Trans. Inst. Electron. Inf. Commun. Eng. E **74**, 3334 (1991).

[19] J.-P. Zhang and K. Petermann, IEEE J. Quantum Electron. **30**, 1529 (1994).

[20] A. Valle, J. Sarma, and K. A. Shore, Opt. Commun. **115**, 297 (1995); IEEE J. Quantum Electron. **31**, 1423 (1995).

[21] J. Y. Law and G. P. Agrawal, IEEE J. Quantum Electron. **33**, 462 (1997).

[22] H. K. Bissessur, F. Koyama, and K. Iga, IEEE J. Sel. Top. Quantum Electron. **3**, 344 (1997).

[23] L. E. Thode *et al.*, in *Physics and Simulation of Optoelectronic Devices II*, edited by W. W. Chow and M. Osinski, SPIE Proc. No. 2146 (SPIE, Bellingham, 1994), p. 174; L. E. Thode *et al.*, in *Physics and Simulation of Optoelectronic Devices III*, edited by M. Osinski and W. W. Chow, SPIE Proc. No. 2399 (SPIE, Bellingham, 1995), p. 348.

[24] G. R. Hadley *et al.*, in *Physics and Simulation of Optoelectronic Devices III*, (Ref. [23]), p. 336; IEEE J. Quantum Electron. **32**, 607 (1996).

[25] Y.-G. Zhao and J. G. McInerney, IEEE J. Quantum Electron. **32**, 1950 (1996).

[26] Z.-M. Li, in *Physics and Simulation of Optoelectronic Devices V*, edited by M. Osinski and W. W. Chow, SPIE Proc. No. 2994 (SPIE, Bellingham, 1997), p. 698.

[27] C. Z. Ning, R. A. Indik, and J. V. Moloney, J. Opt. Soc. Am. B **12**, 1993 (1995); C. Z. Ning, R. A. Indik, J. V. Moloney, and S. W. Koch, in *Physics and Simulation of Optoelectronic Devices III*, (Ref. [23]), p. 617.
[28] C. Z. Ning and J. V. Moloney, Appl. Phys. Lett. **66**, 559 (1995).
[29] C. Z. Ning and J. V. Moloney, Opt. Lett. **20**, 1151 (1995).
[30] G. R. Hadley, Opt. Lett. **20**, 1483 (1995).
[31] C. Z. Ning, R. A. Indik, and J. V. Moloney, IEEE J. Quantum Electron. **33**, 1543 (1997).
[32] P. K. Jakobsen, J. V. Moloney, A. C. Newell, and R. Indik, Phys. Rev. A **45**, 8129 (1992).
[33] D. Burak and R. Binder, IEEE J. Quantum Electron. **33**, 1205 (1997).
[34] On the other hand, the field polarization has already been treated in the context of a VCSEL model that was originally introduced in Ref. [35] with contributions from one of the present authors (J. V. M.) and recently developed further by San Miguel *et al.* [36]. However, we feel that the four-level system approach to the optical response used in this model is not suited for adequately describing a semiconductor quantum well VCSEL. Since the emphasis of the present paper is the role of gain dispersion in the selection of transverse modes, we found it more important to have a microscopic basis for the susceptibility than to take the vector nature of the field into account. We furthermore note that the case of an index-guided VCSEL — which has not been addressed in the context of this simplified vectorial model — would require a careful consideration of the boundary conditions for the electric field. A notable attempt in that direction is presented in Ref. [37].
[35] M. San Miguel, Q. Feng, and J. V. Moloney, Phys. Rev. B **52**, 1728 (1995).
[36] J. Martín-Regalado *et al.*, Quantum Semiclassic. Opt. **9**, 713 (1997), and references therein.
[37] D. Burak and R. Binder, in *Physics and Simulation of Optoelectronic Devices VI*, edited by M. Osinski, P. Blood, and A. Ishibashi, SPIE Proc. No. 3283 (SPIE, Bellingham, 1998), p. 269.
[38] See, for instance, W. Rudolph and B. Wilhelmi, *Light Pulse Compression* (Harwood, Chur, 1989).
[39] H. Haug and S. W. Koch, *Quantum Theory of the Optical and Electronic Properties of Semiconductors* (World Scientific, Singapore, 1993).
[40] W. W. Chow, S. W. Koch, and M. Sargent III, *Semiconductor Laser Physics* (Springer, New York, 1994).
[41] Y. P. Varshni, Physica **34**, 149 (1967).
[42] F. Jahnke and S. W. Koch, Opt. Lett. **18**, 1438 (1993).
[43] The error introduced by this procedure is second order in Δt with a prefactor of order $\dot{X}$, where X is one of N, T_p, or T_l. One might also be concerned that roundoff error will accumulate, since $\dot{N}$ is extremely small compared to Δt. However, $\dot{N}\Delta t \approx 10^{-6}$, which is still adequately resolved in double precision.
[44] Y. Kaneko *et al.*, Jpn. J. Appl. Phys., Part 2 **L32**, 1612 (1993).
[45] T. J. Rogers *et al.*, IEEE Photonics Technol. Lett. **7**, 238 (1995).
[46] G. Hasnain *et al.*, IEEE J. Quantum Electron. **27**, 1377 (1991).
[47] For a related discussion of boundary effects in large-aspect-ratio lasers, see G. K. Harkness *et al.*, Phys. Rev. A **50**, 4310 (1994).
[48] M. Sargent III, M. O. Scully, and W. E. Lamb, *Laser Physics* (Addison-Wesley, London, 1974).
[49] K. L. Lear, K. D. Choquette, R. P. Schneider, Jr., and S. P. Kilcoyne, Appl. Phys. Lett. **66**, 2616 (1995).
[50] K. D. Choquette and R. E. Leibenguth, IEEE Photonics Technol. Lett. **6**, 40 (1994).
[51] H. Li, T. L. Lucas, J. G. McInerney, and R. A. Morgan, Chaos Solitons Fractals **4**, 1619 (1994).